On the pressure effect in energetic deposition of Cu thin films by modulated pulsed power magnetron sputtering: A global plasma model and experiments

B. C. Zheng, D. Meng, H. L. Che, and M. K. Lei

Articles you may be interested in

Preliminary study of CdTe and CdTe:Cu thin films nanostructures deposited by using DC magnetron sputtering
AIP Conf. Proc. **1555**, 48 (2013); 10.1063/1.4820991

Study of Ni 2 – Mn – Ga phase formation by magnetron sputtering film deposition at low temperature onto Si substrates and La Ni O 3 ∕ Pb (Ti , Zr) O 3 buffer
J. Vac. Sci. Technol. A **28**, 6 (2010); 10.1116/1.3256200

Influence of deposition pressure and rf power on the structure and electrical properties of Zr 0.8 Sn 0.2 Ti O 4 thin films prepared by rf magnetron sputtering
J. Vac. Sci. Technol. B **25**, 299 (2007); 10.1116/1.2437153

Interdependence between stress, preferred orientation, and surface morphology of nanocrystalline TiN thin films deposited by dual ion beam sputtering
J. Appl. Phys. **99**, 113519 (2006); 10.1063/1.2197287

Stress evolution during and after sputter deposition of Cu thin films onto Si (100) substrates under various sputtering pressures
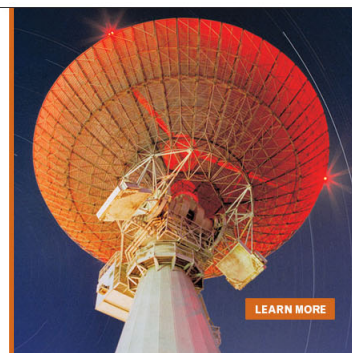J. Appl. Phys. **97**, 054908 (2005); 10.1063/1.1858062

On the pressure effect in energetic deposition of Cu thin films by modulated pulsed power magnetron sputtering: A global plasma model and experiments

B. C. Zheng, D. Meng, H. L. Che, and M. K. Lei[a]

Surface Engineering Laboratory, School of Materials Science and Engineering, Dalian University of Technology, Dalian 116024, China

The modulated pulsed power magnetron sputtering (MPPMS) discharge processes are numerically modeled and experimentally investigated, in order to explore the effect of the pressure on MPPMS discharges as well as on the microstructure of the deposited thin films. A global plasma model has been developed based on a volume-averaged global description of the ionization region, considering the loss of electrons by cross-B diffusion. The temporal variations of internal plasma parameters at different pressures from 0.1 to 0.7 Pa are obtained by fitting the model to duplicate the experimental discharge data, and Cu thin films are deposited by MPPMS at the corresponding pressures. The surface morphology, grain size and orientation, and microstructure of the deposited thin films are investigated by scanning electron microscopy, transmission electron microscopy, and x-ray diffraction. By increasing the pressure from 0.1 to 0.7 Pa, both the ion bombardment energy and substrate temperature which are estimated by the modeled plasma parameters decrease, corresponding to the observed transition of the deposited thin films from a void free structure with a wide distribution of grain size (zone T) into an underdense structure with a fine fiber texture (zone 1) in the extended structure zone diagram (SZD). The microstructure and texture transition of Cu thin films are well-explained by the extended SZD, suggesting that the primary plasma processes are properly incorporated in the model. The results contribute to the understanding of the characteristics of MPPMS discharges, as well as its correlation with the microstructure and texture of deposited Cu thin films. © *2015 AIP Publishing LLC*.
[http://dx.doi.org/10.1063/1.4921443]

I. INTRODUCTION

High power impulse magnetron sputtering (HiPIMS) has been known as a promising energetic deposition technique developed in recent years.[1,2] A high plasma density of 10^{18}–$10^{19} m^{-3}$ during HiPIMS discharges is generated by applying unipolar pulses at high power density and low duty cycle to the magnetron target,[3,4] while the average power is kept about 2 orders of magnitude lower than the peak power to avoid magnetron overheating and target melting.[5] The sputtered metal atoms could be the dominant species with a high ionization fraction up to 90%,[6,7] the resulting ionized flux provides a better control of the thin film growth and a uniform deposition on complex structures by accelerating the ionized species across the plasma sheath.[8–10] The adatom mobility is enhanced and the deposited species are incorporated into the substrate at increased impact energy,[11] leading to a smooth and dense thin film with improved adhesion.[12,13] However, the lower deposition rate of HiPIMS compared with conventional magnetron sputtering techniques is the major drawback.[14–16]

As a variation of the HiPIMS technique, the modulated pulsed power magnetron sputtering (MPPMS)[17] provides a high ionization fraction of sputtered species while at the same time achieving a high deposition rate,[18,19] by using a longer but lower pulsed power that comprised many micropulses. The shape and magnitude of the long pulses, also known as the macropulses, can be arbitrarily controlled by modulating the duty cycle of the micropulses, thus providing more flexible control than HiPIMS.[20] MPPMS processes have been successfully applied to deposit elementary,[21] multilayer,[22,23] as well as nanocomposite[24] coatings with excellent mechanical and wear resistance.

The newly introduced deposition parameters and the pulsed operation of HiPIMS and MPPMS provide a wider range of process parameters and pulse parameters.[2,25] However, the difficulty of the selection and optimization of these primary parameters is increased as well, due to the influence of the externally primary parameters on the internal plasma parameters, thus on the thin film structure during HiPIMS and MPPMS discharges is not fully understood. For example, the pressure plays a key role in influencing the thin film deposition in conventional magnetron sputtering[26] as well as in HiPIMS technique[27–29] and has been selected as one of the most significant parameters in structure zone diagram (SZD) proposed by Thornton.[30] However, for the energetic depositions such as HiPIMS and MPPMS, the internal plasma parameters during the discharge are significantly influenced by the pressure, and the relationship between the pressure and the thin film growth remains unclear.

Since the internal plasma parameters are often hard to measure near the racetrack of the target,[31] several models have been developed for the HiPIMS discharges.[14,32–37] A

[a] Author to whom correspondence should be addressed. Electronic mail: mklei@dlut.edu.cn

phenomenological pathways model for HiPIMS discharges was proposed by Christie[32] and improved by Vlcek and Burcalova[33] to describe the discharge process and explain the deposition rate loss. Besides, an ionization region model (IRM) is developed to explore the internal discharge physics during HiPIMS pulse,[34] such as the temporal variation of plasma parameters,[14,35] the heating mechanism,[36] and the development of self-sputtering.[37] However, these aforementioned models are not appropriate descriptions for the MPPMS discharge, which possesses various ionization periods during one modulated macropulse.

In this study, an Ar/Cu MPPMS process is numerically modeled and experimentally investigated, in order to explore the influence of the pressure on the internal plasma parameters and thus on the microstructure of deposited thin films during MPPMS discharges. A time-dependent global plasma model is developed for MPPMS discharges based on a volume-averaged global description of the ionization region, considering the loss of electrons by cross-B diffusion. The temporal variations of internal plasma parameters, such as number densities of each species, electron temperature, ionization fraction, and potential drop across the ionization region, can be obtained by fitting the model to duplicate the experimental discharge data at different pressures. The surface morphology, grain size and orientation, and microstructure of the Cu thin films deposited by MPPMS under the corresponding conditions are investigated by scanning electron microscopy (SEM), transmission electron microscopy (TEM), and x-ray diffraction (XRD). The microstructure and texture transition of thin films with the internal plasma parameters can be well-explained by the extended SZD, suggesting that the primary plasma processes are properly incorporated in the model.

II. EXPERIMENTAL DETAILS

Cu thin films were deposited in a closed-field unbalanced magnetron sputtering system equipped with four rectangular shaped unbalanced magnetrons. Cu sputtering target of 99.95% purity with an area of $440 \times 140 \, mm^2$ and a thickness of 6 mm was powered by a Zpulser AXIA™ MPPMS power supply at an average power of 2 kW. The waveforms of discharge voltages and currents were monitored and recorded by a Tektronix TDS 2014C digital oscilloscope and the Zpulser operating software. The experiments were performed at a base pressure below 2×10^{-4} Pa, using the argon with 99.99% purity as the working gas, which was supplied to adjust the pressures ranging from 0.1 to 0.7 Pa.

The pulse shapes of discharges can be arbitrarily tailored by manipulating the micropulse on-time τ_{on} and off-time τ_{off}. Fig. 1 shows the typical experimental MPPMS pulses of the discharge voltage, current, and power during one modulated macropulse at 0.3 Pa, under the micropulse configuration τ_{off}/τ_{on} of 34/6 μs during the first 450 μs and 10/20 μs during the last 250 μs, respectively, at a charge voltage of -600 V. A high density plasma and a stable discharge process are thereby achieved by first introducing a weakly ionized period of 450 μs to ignite the plasma followed by a transition to the strongly ionized period of 250 μs.
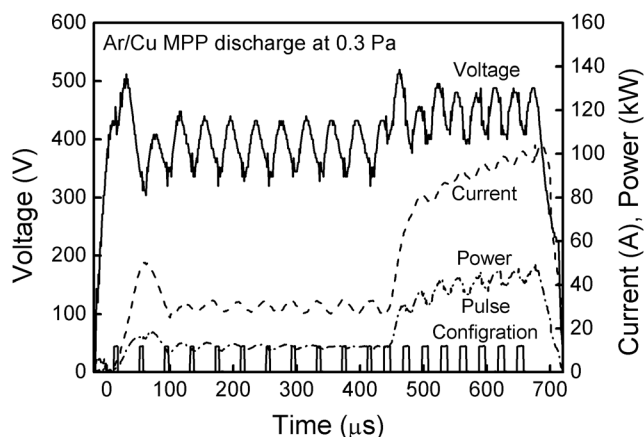

FIG. 1. Typical experimental MPPMS pulses of the discharge voltage (V), current (A), power (kW), and micropulse configuration during one modulated macropulse. A Cu cathode was sputtered by Ar gas at 0.3 Pa.

Fig. 2 shows the experimental discharge currents during the modulated macropulses of 700 μs at different pressures of 0.1–0.7 Pa, the discharge voltages at all pressures are similar to each other as shown in Fig. 1. A delay of about 50 μs in discharge current is observed at 0.1 Pa, due to the secondary electrons need more time to cause ionization of the gas at lower pressure.[5] The discharge currents at all pressures are around 30 A during the weakly ionized period of the first 450 μs, and go up with the pressure during the strongly ionized period of the last 250 μs. A jump in the current appears between 0.1 and 0.3 Pa, due to the fewer electron-atom impact ionizations at 0.1 Pa.

Si(100) wafers were adopted as the substrate, which were ultrasonically cleaned first in acetone then in ethanol for 30 min, respectively. The substrates were mounted on a substrate holder with a distance of 100 mm to the target. In order to remove the surface contamination, the substrates were cleaned by Ar^+ etching at 2.5 Pa for 20 min by using a pulsed dc bias of -350 V with 100 kHz and 90% duty cycle.

The Cu thin films with a same thickness of 1.7 μm were deposited by MPPMS in the pressure range of 0.1 Pa to 0.7 Pa, which is selected due to its practical significance. The
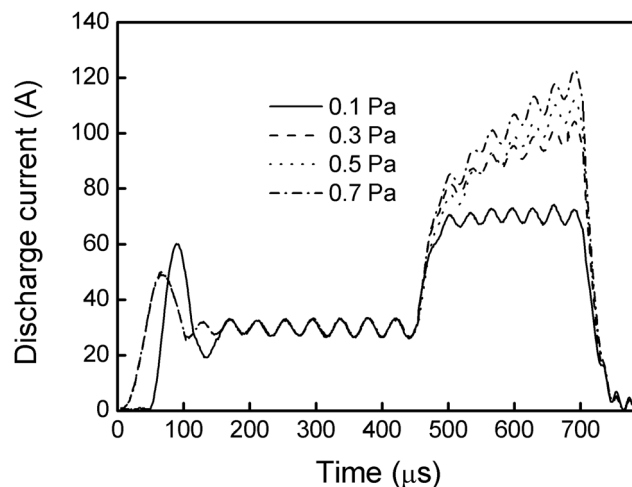

FIG. 2. Experimental discharge currents during the modulated macropulses of 700 μs at different pressures of 0.1–0.7 Pa.

MPPMS discharges are hard to be maintained at the pressures lower than 0.1 Pa, and the quality of the deposited Cu thin films is unacceptable at the pressures higher than 0.7 Pa. The surface morphology and the microstructure of the deposited Cu thin films were investigated by using ZEISS SUPRA 55-32-76 field-emission SEM (FE-SEM) with an operating voltage of 15 kV, and by Tecnai G2 20 S-TWIN TEM with an accelerated voltage of 200 kV. The samples for TEM observation were glued together with the thin film surfaces facing each other using M-bond 610 adhesive and clamped till the epoxy was cured. The cured samples were ground mechanically to foils with a thickness of about 30 μm. The foils were further thinned down to electron transparency using a Gatan Model 694 precision ion polishing with a 5 keV Ar$^+$ beam at an angle of 8°. The crystal structure of the deposited Cu thin film was characterized using monochromatic Cu-K$_\alpha$ radiation on a PANalytical EMPYREAN XRD.

III. MODEL DESCRIPTION

A time-dependent global plasma model is developed based on previous modeling works of steady-state[38,39] and pulsed plasma discharges,[34,40–42] in order to explore the underlying plasma physics during MPPMS discharges. The model operates by solving a set of coupled differential equations which are similar to those given in detail by Raadu et al.[34] However, in the present model, the electron loss across the magnetic field is considered and assumed as Bohm diffusion, and the time-dependent potential drop across the ionization region U_{IR} can be obtained by solving the Poisson equation. Using U_{IR} to represent the time-dependent effective power transfer coefficient F_{PWR} and average ion return fraction β, and fitting the Bohm diffusion coefficient of electrons to reproduce the experimental discharge waveforms, the temporal variation of internal plasma parameters during one modulated macropulse of the MPPMS discharge which corresponds to the real physical situation can be obtained. The detailed presentation is as follows.

To establish the global plasma model, the primary species and the key reactions during the discharge should be identified first. At the low working pressures used in the MPPMS discharges, the electrons are far from being in thermal equilibrium and the Maxwellian equilibrium assumption fails. In order to consider the kinetic effects of energetic electrons both in the power coupling to the discharge and in the ionization processes, the electrons are split up into two populations, i.e., the hot electron species originated from the secondary emitted electrons, and the cold electrons produced mainly by ionization in the plasma.[36] For the Ar/Cu MPPMS discharge, the primary species include electron e, hot electron e^H, atomic Ar and Cu, hot atom Ar^H, metastable Ar^m, ionized Ar$^+$ and Cu$^+$. Fig. 3 shows the schematic diagram of the model geometry, the particle balances, and the corresponding reactions in the ionization region. The ionization region with a semi-torus shape hovers above the rectangular racetrack of the target, radius $R = 1.5$ cm and circumference $l = 100$ cm, based on the experimental observation of the high density discharging torus, the racetrack erosion area,
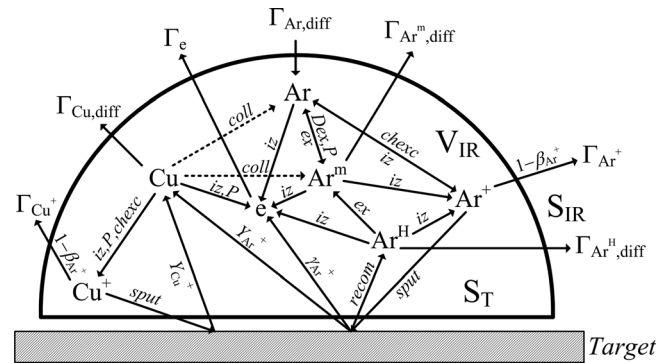

FIG. 3. Schematic diagram of the model geometry, the particle balances, and the corresponding reactions in the ionization region. The subscripts denote the following: diff (diffusion), IR (ionization region), T (target), iz (ionization), ex (excitation), Dex (de-excitation), P (Penning ionization), chexc (charge exchange), coll (collision), recom (recombination), and sput (sputtering).

and the magnetic field distribution. The surface area and volume of the ionization region S_{IR} and V_{IR}, and the contact area of the ionization region with target S_T can be expressed as

$$
\begin{aligned}
S_{IR} &= (\pi R + 2R)l, \\
V_{IR} &= \frac{\pi R^2}{2}l, \\
S_T &= 2Rl.
\end{aligned}
\tag{1}
$$

In the ionization region, the working gas Ar may be ionized or excited by colliding with energetic electrons, the Cu atoms sputtered from the target by Ar$^+$ bombardment may be ionized by electron impact ionization and attracted back to sputter the Cu target. Owing to the lack of cross-section data for the ionization of excited Cu, the ionized Cu$^+$ is assumed only generated by the single-step electron impact ionization, Cu + e → Cu$^+$ + 2 e, and by Penning ionization, Cu + Ar^m → Cu$^+$ + Ar + e. The return flux of recombined Ar$^+$ from the target is treated as the hot argon species with an equivalent temperature same as the sputtered Cu. The diffusion losses across the boundary of the ionization region are governed by their thermal velocity for the neutrals, Bohm velocity for the ion fluxes reduced by the ion return fraction β, and Bohm diffusion for the electrons. The losses across the boundary and the interactions of these species are shown in Fig. 3.

A. Potential drop across the ionization region

In magnetron sputtering discharges, the electrons are trapped in the vicinity of the cathode target to form an additional ionization region and increase the plasma density. In order to maintain the quasi-neutrality of the plasma in the ionization region, a potential drop U_{IR} with typically up to 10%–20% of the applied discharge voltage U_D exists across the plasma outside the cathode sheath, which has been observed in dcMS,[43] HiPIMS,[31,44] and MPPMS[45] discharges. The electric field generated by the potential drop extends from the cathode sheath to a distance of several centimeters in the bulk plasma and is assumed as constant in the

ionization region. Fig. 4 shows the schematic diagram of the region division and the electric potential distribution used in the model. The potential drop U_{IR} adds an electron heating mechanism, namely, the direct Ohmic heating $U_{IR}\langle I_e\rangle$,[36] in addition to the secondary electron heating. Here, $\langle I_e\rangle$ is the volume average of the electron current inside the ionization region, and $U_{SH} = U_D - U_{IR}$ is the potential drop across the sheath.

According to the estimation by Brenning *et al.*,[14] the discharge current across the ionization region gradually transforms from ion current domination near the sheath to electron current domination near the bulk plasma. Approximating $\langle I_e\rangle \approx I_D/2$, the effective power transfer coefficient F_{PWR}, which represents the fraction of input power effectively transferred to heat the electrons, can be expressed as[36]

$$F_{PWR} = \frac{eV_{IR}E_{htc}\nu_{iz}^H + U_{IR}\cdot\langle I_e\rangle}{P_D} = \frac{eV_{IR}E_{htc}\nu_{iz}^H + U_{IR}\cdot I_D/2}{U_D I_D},$$

(2)

where e is the elementary charge, $E_{htc} = 10\,\text{eV}$ is the hot-to-cold population energy transfer when a new electron being created by the hot electron ionization collision falls into the energy range of the cold population,[36] I_D and P_D are the discharge current and the power input, respectively, and

$$\nu_{iz}^H = n_{e^H}(k_{iz}^H(n_{Ar} + n_{Ar^H}) + k_{miz}^H n_{Ar^m} + k_{Miz}^H n_{Cu}),$$

(3)

where ν_{iz}^H is the ionization frequency of the hot electrons with each species, k and n are the rate coefficients and the number densities of the corresponding reactions and species, respectively.

During the discharge, a significant portion of the ionized species is back-attracted to the target due to the potential drop U_{IR} outside the cathode sheath. In order to estimate the ion return fraction, assuming the ionization probability of sputtered species is constant over the ionization region, and the ionized species i flow away from the ionization region against the potential drop with an equivalent temperature T_i. The average energy of the sputtered Cu atoms are calculated using the transport of ions in matter (TRIM) software,[46] and the gas temperature is assumed as $0.026\,\text{eV}$. Under these simplified assumptions, one can derive that the species
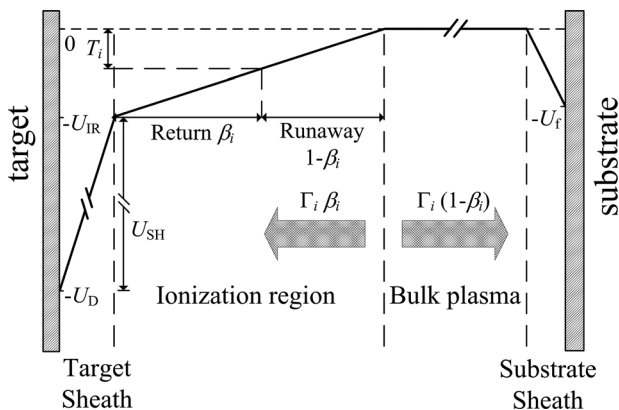

FIG. 4. Schematic diagram of the region division, the electric potential distribution, and the probability of ion return and runaway in the model.

would be back-attracted if the ionization occurs at the position where the equivalent temperature T_i is not sufficient to overcome the remnant potential drop, otherwise the ions would runaway from the ionization region. The average ion return fraction β_i can be expressed as

$$\beta_i = \begin{cases} 0 & U_{IR} \leq T_i \\ 1 - \dfrac{T_i}{U_{IR}} & U_{IR} > T_i \end{cases} \quad i = \text{Cu}^+, \text{Ar}^+.$$

(4)

The ion return and runaway fluxes are demonstrated in Fig. 4.

B. Particle balance

By considering the generation and the loss of each species as shown in Fig. 3, the rate equations which describe the time-dependent particle densities can be obtained as follows.

1. Particle balance for Ar species

The rate equation for the working gas Ar is

$$\begin{aligned}
\frac{dn_{Ar}}{dt} = &-\left(k_{iz}n_e + k_{iz}^H n_{e^H}\right)n_{Ar} - \left(k_{ex}n_e + k_{ex}^H n_{e^H}\right)n_{Ar} \\
&- \Gamma_{Cu,coll}\frac{m_{Cu}}{m_{Ar}}\frac{n_{Ar}}{n_{Ar} + n_{Ar^m}}\frac{S_{IR} - S_T}{V_{IR}} \\
&+ k_{chexc}n_{Ar^+}n_{Cu} + k_P n_{Ar^m}n_{Cu} \\
&+ \left(k_{dex}n_e + k_{dex}^H n_{e^H}\right)n_{Ar^m} + \Gamma_{Ar,diff}\frac{S_{IR} - S_T}{V_{IR}},
\end{aligned}$$

(5)

where m and Γ are the masses and the fluxes of the corresponding species, respectively. The first three terms on the right hand side are the losses of argon by electron impact ionization and excitation, and by collisions with the sputtering wind, the last four terms are the gains of argon by charge exchange of Ar$^+$-Cu, Penning ionization of Ar^m-Cu, de-excitation, and diffusional refill of Ar from the surroundings. Following Raadu *et al.*,[34] the effect of sputtering wind on the Ar gas is treated as the momentum exchange collision with sputtered fluxes of metal atoms and ions $\Gamma_{cu,coll}$. This fraction of Cu momentum flow is balanced by an Ar outflow across the surface $(S_{IR} - S_T)$, considering the mass difference between Ar and Cu species, and the momentum loss goes to the metastable Ar^m. The diffusional refill of Ar from the surroundings is described by a flux density $\Gamma_{Ar,diff}$, which is determined by the density difference of Ar into and out of the ionization region. The rate coefficients $k(T_e)$ are listed, the sputtering wind and the diffusional refill $\Gamma_{Ar,diff}$ are discussed in more detail in the Appendix.

For Ar$^+$ ions, the rate equation can be written as

$$\begin{aligned}
\frac{dn_{Ar^+}}{dt} = &-k_{chexc}n_{Ar^+}n_{Cu} - \Gamma_{Ar^+}\frac{S_T + (S_{IR} - S_T)(1 - \beta_{Ar^+})}{V_{IR}} \\
&+ \left(k_{iz}n_e + k_{iz}^H n_{e^H}\right)(n_{Ar} + n_{Ar^H}) \\
&+ \left(k_{miz}n_e + k_{miz}^H n_{e^H}\right)n_{Ar^m}.
\end{aligned}$$

(6)

The first line on the right hand side includes the losses of Ar$^+$ by charge exchange of Ar$^+$-Cu and diffusion out of the ionization region and the second line includes the generation

of Ar^+ by electron impact ionization of Ar, Ar^H, and Ar^m. The flux of Ar^+ ions out of the ionization region is Γ_{Ar^+} across the surface S_T and is reduced by a fraction β_{Ar^+} across the surface $(S_{IR} - S_T)$. This term is discussed in more detail in the Appendix.

Similar to the Ar atoms, the rate equation for Ar^m can be written as

$$\frac{dn_{Ar^m}}{dt} = -\left(k_{miz}n_e + k_{miz}^H n_{e^H}\right)n_{Ar^m} - k_P n_{Ar^m} n_{Cu}$$
$$- \left(k_{dex}n_e + k_{dex}^H n_{e^H}\right)n_{Ar^m} - \Gamma_{Ar^m,diff}\frac{S_{IR} - S_T}{V_{IR}}$$
$$- \Gamma_{Cu,coll}\frac{m_{Cu}}{m_{Ar}}\frac{n_{Ar^m}}{n_{Ar} + n_{Ar^m}}\frac{S_{IR} - S_T}{V_{IR}}$$
$$+ \left(k_{ex}n_e + k_{ex}^H n_{e^H}\right)(n_{Ar} + n_{Ar^H}) \qquad (7)$$

and for Ar^H atoms, ignoring the effect of sputtering wind and considering the recombination of Ar^+ on the target

$$\frac{dn_{Ar^H}}{dt} = -\left(k_{iz}n_e + k_{iz}^H n_{e^H}\right)n_{Ar^H} - \left(k_{ex}n_e + k_{ex}^H n_{e^H}\right)n_{Ar^H}$$
$$- \Gamma_{Ar^H,diff}\frac{S_{IR} - S_T}{V_{IR}} + \Gamma_{Ar^+}\frac{S_T}{V_{IR}}. \qquad (8)$$

The last term is the recombination of Ar^+ on the target, assuming all the Ar^+ ions impact on the target are recombined and return to the ionization region.

2. Particle balance for Cu species

The rate equation for Cu atoms is

$$\frac{dn_{Cu}}{dt} = -\left(k_{Miz}n_e + k_{Miz}^H n_{e^H}\right)n_{Cu} - k_P n_{Ar^m} n_{Cu}$$
$$- k_{chexc}n_{Ar^+}n_{Cu} - \Gamma_{Cu,diff}\frac{S_{IR} - S_T}{V_{IR}}$$
$$+ \left(\Gamma_{Ar^+}Y_{Ar^+} + \Gamma_{Cu^+}Y_{Cu^+}\right)\frac{S_T}{V_{IR}}. \qquad (9)$$

The first line on the right hand side includes the losses of Cu by electron impact ionization, Penning ionization of Ar^m-Cu, charge exchange of Ar^+-Cu, and diffusion out of the ionization region. The diffusion term is discussed in the Appendix. The last term is the generation of Cu atoms by the sputtering of Ar^+ and Cu^+ from the target. Y_{Ar^+} and Y_{Cu^+} are the sputtering yields of Ar^+ and Cu^+ with the Cu target calculated by the TRIM software,[46] respectively.

Similar to Ar^+, the rate equation for Cu^+ ions is

$$\frac{dn_{Cu^+}}{dt} = \left(k_{Miz}n_e + k_{Miz}^H n_{e^H}\right)n_{Cu} + k_P n_{Ar^m}n_{Cu} + k_{chexc}n_{Ar^+}n_{Cu}$$
$$- \Gamma_{Cu^+}\frac{S_T + (S_{IR} - S_T)\cdot(1 - \beta_{Cu^+})}{V_{IR}}. \qquad (10)$$

3. Particle balance for electrons

The continuity equation for the electrons is

$$\frac{dn_e}{dt} = \Sigma_e - \Gamma_e\frac{S_{IR} - S_T}{V_{IR}}, \qquad (11)$$

where Σ_e is the volume-averaged electron source

$$\Sigma_e = (k_{iz}n_e + k_{iz}^H n_{e^H})(n_{Ar} + n_{Ar^H}) + (k_{miz}n_e + k_{miz}^H n_{e^H})n_{Ar^m}$$
$$+ (k_{Miz}n_e + k_{Miz}^H n_{e^H})n_{Cu} + k_P n_{Cu}n_{Ar^m}, \qquad (12)$$

which includes the electron impact ionization of Ar, Ar^H, Ar^m, and Cu, and the Penning ionization of Ar^m-Cu. The second term on the right hand side of Eq. (11) is the loss of electrons across the surface $(S_{IR} - S_T)$. The electron flux can be derived from the drift-diffusion approximation as

$$\Gamma_e = D_e\nabla n_{el} + \frac{D_e}{T_e}n_{el}\boldsymbol{E} \approx \frac{D_e}{R}n_{el}\left(1 + \frac{U_{IR}}{T_e}\right). \qquad (13)$$

At the pressures of 0.1–0.7 Pa presented here, the mean free path of momentum exchange λ_{coll} is larger than the characteristic size of the ionization region R (the estimation is given in Appendix), and the electron density on the ionization region boundary can be assumed as $n_{el} = 0.4 n_e$, according to the collisionless Langmuir solution for infinite cylinder geometry.[47] $\boldsymbol{E} = U_{IR}/R$ is the constant electric field, and the Bohm diffusion coefficient of electrons is

$$D_e = \frac{1}{\omega_{ge}\tau_c}\frac{T_e}{B}. \qquad (14)$$

The gyration-to-collision frequency ratio $\omega_{ge}\tau_c$ is the fitting parameter in this model, T_e is the electron temperature, and $B = 800\,G$ is the magnetic field at the ionization region boundary measured in the experiment.

The rate equation of the hot electrons can be expressed as[36]

$$\frac{dn_{e^H}}{dt} = \frac{1}{eU_D/2}\left(\frac{U_{SH}\cdot I_{se}}{V_{IR}} - Q^H\right), \qquad (15)$$

where I_{se} is the secondary electron current

$$I_{se} = eS_T(\gamma_{Ar^+}\Gamma_{Ar^+} + \gamma_{Cu^+}\Gamma_{Cu^+}), \qquad (16)$$

where γ_i and Γ_i are the secondary electron emission coefficient and the flux of the i species impacting the target, respectively. The value $\gamma_{Ar^+} = 0.112$ is obtained by using an empirical formula $\gamma_{Ar^+} = 0.016(E_{iz,Ar} - 2\varphi)$ for the Ar^+ ion,[47] where $E_{iz,Ar}$ is the ionization energy of Ar and φ is the work function of the target material. The coefficient γ_{Cu^+} by the self-sputtering of Cu^+ is negligible and assumed to be 0. Q^H is the energy loss of hot electrons due to inelastic collisions with Ar, Ar^H, Ar^m, and Cu

$$\frac{Q^H}{e} = (E_{Ar,c} + E_{htc})k_{iz}^H n_{e^H}(n_{Ar} + n_{Ar^H})$$
$$+ (E_{Ar^m,c} + E_{htc})k_{miz}^H n_{e^H}n_{Ar^m}$$
$$+ (E_{Cu,c} + E_{htc})k_{Miz}^H n_{e^H}n_{Cu} - E_{dex}k_{dex}^H n_{e^H}n_{Ar^m}. \qquad (17)$$

4. Poisson equation

The time-dependent potential drop U_{IR} maintains the quasi-neutrality of the plasma and can be obtained by solving

the Poisson equation. Under the assumption of a constant electric field in the ionization region, the Poisson equation can be simplified as

$$U_{IR} = -\frac{e \cdot R^2}{\varepsilon_0}(n_{Ar^+} + n_{Cu^+} - n_e - n_{e^H}). \qquad (18)$$

5. Energy balance

The electrons are assumed in thermal equilibrium, and the time-dependent electron temperature T_e can be obtained by solving the energy balance equation of the system. The variation of electron energy density with time is

$$\frac{d}{dt}\left(\frac{3}{2}en_eT_e\right) = F_{PWR}\frac{P_D(t)}{V_{IR}} - Q - \left(\frac{3}{2}eT_e\Gamma_e\frac{S_{IR} - S_T}{V_{IR}}\right.$$
$$\left. + \sum_{i=Ar^+,Cu^+}\frac{1}{2}eT_e\Gamma_i\frac{S_T + (S_{IR} - S_T)(1 - \beta_i)}{V_{IR}}\right). \qquad (19)$$

The first term on the right hand side is the external power input, Q is the energy loss of electrons due to inelastic collisions, and the last term is the energy loss of charged particles by leaving the ionization region, including the energy loss of $(3/2)eT_e$ per electron and $(1/2)eT_e$ per ion. Substituting the electron continuity equation (11)–(19),

$$\frac{3}{2}n_e\frac{dT_e}{dt} = E_{htc}\nu_{iz}^H + \frac{I_DU_{IR}/2}{eV_{IR}}$$
$$- \sum_{i=Ar^+,Cu^+}\frac{\Gamma_i}{2}T_e\frac{S_T + (S_{IR} - S_T)(1 - \beta_i)}{V_{IR}}$$
$$- \frac{Q}{e} - \frac{3}{2}T_e\Sigma_e. \qquad (20)$$

Q includes the energy losses by electron impact ionization of Ar, Ar^m, Ar^H, and Cu, the energy gains by de-excitation of Ar^m and Penning ionization of Ar^m-Cu

$$\frac{Q}{e} = E_{Ar,c}k_{iz}n_e(n_{Ar} + n_{Ar^H}) + E_{Ar^m,c}k_{miz}n_en_{Ar^m}$$
$$+ E_{Cu,c}k_{Miz}n_en_{Cu} - E_{dex}k_{dex}n_en_{Ar^m} - E_Pk_Pn_{Cu}n_{Ar^m}, \qquad (21)$$

where

$$k_{iz}E_{Ar,c} = k_{iz}E_{iz} + k_{ex}E_{ex} + k_{el}\frac{3m_e}{m_{Ar}}T_e,$$
$$k_{miz}E_{Ar^m,c} = k_{miz}E_{miz} + k_{el}\frac{3m_e}{m_{Ar}}T_e, \qquad (22)$$
$$k_{Miz}E_{Cu,c} = k_{Miz}E_{Miz} + k_{Mel}\frac{3m_e}{m_{Cu}}T_e.$$

Here, $E_{Ar,c}$, $E_{Ar^m,c}$, and $E_{Cu,c}$ are the collisional energy losses per electron-ion pair created of Ar, Ar^m, and Cu, E_{dex} and E_P are the threshold energies of Ar^m-e de-excitation and Ar^m-Cu Penning ionization, respectively.

Considering the ion and the secondary electron fluxes above the racetrack, the calculated discharge current can be represented as
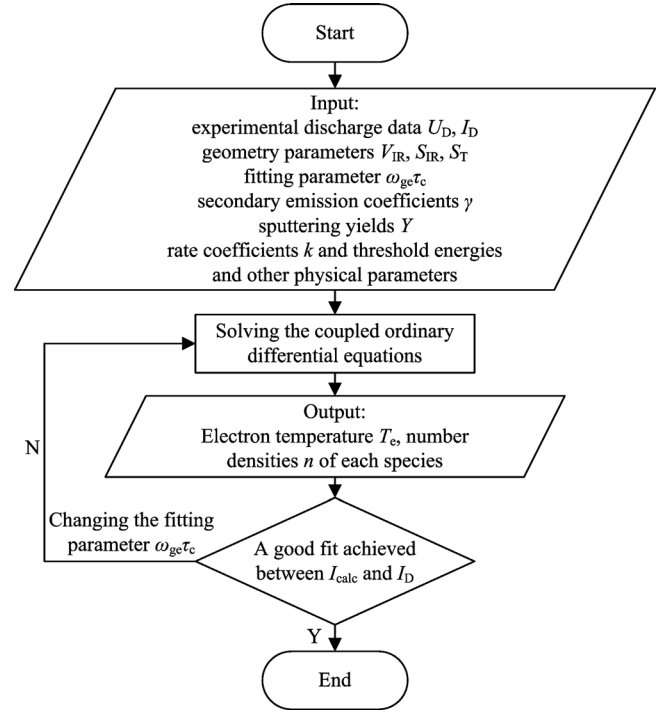

FIG. 5. Flow chart of the numerical procedure of the global plasma model.

$$I_{calc} = e\Gamma_{Ar^+}S_T(1 + \gamma_{Ar^+}) + e\Gamma_{Cu^+}S_T(1 + \gamma_{Cu^+}). \qquad (23)$$

Fig. 5 shows the flow chart of the numerical procedure of the global plasma model. Using the experimental data of discharge voltages and currents as the input parameters, the discharge currents are reproduced by operating the model and fitting the gyration-to-collision frequency ratio $\omega_{ge}\tau_c$. Fig. 6 shows the experimental and the corresponding modeled discharge currents during the modulated macropulses of $700\,\mu s$ at the pressure of 0.3 Pa. By varying the fitting parameter $\omega_{ge}\tau_c$ from 8 to 24, a good current fit is obtained at $\omega_{ge}\tau_c = 16$, which means the modeled discharge process during one macropulse is constrained to be consistent with the real physical situation. Recent modeling work shows that for different set of parameters, such as voltage amplitude, pulse
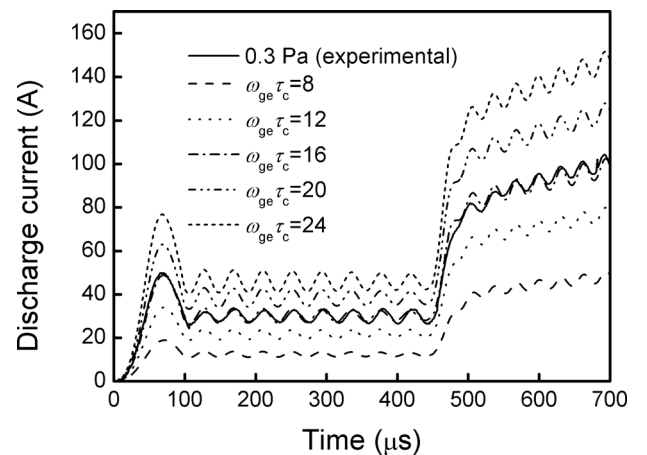

FIG. 6. Experimental and the corresponding modeled discharge currents during the modulated macropulses of $700\,\mu s$ at the pressure of 0.3 Pa, the fitting parameters $\omega_{ge}\tau_c$ is from 8 to 24.

lengths and target materials a nice behavior of the model can be observed as well. However, it is also shown that in some cases an additional fitting parameter, i.e., the secondary electron recapture probability may be needed in order to achieve a good fit, albeit one parameter is sufficient for the chosen parameters presented here. In-depth discussion of this issue is beyond the scope of this paper.

Due to some assumed parameters in the model, one question arises as to the robustness of the solution with respect to these assumed values. Fig. 7 shows the sensitivity analysis of the modeling at 0.3 Pa. The key model output parameter, U_{IR}, which is relatively stable during the macropulse, is averaged over the modulated macropulse of 700 μs and selected as the representation of the sensitivity of the model. By changing each assumed parameter and fitting $\omega_{ge}\tau_c$ to reproduce the experimental discharge current, the variations of U_{IR} with respect to the assumed parameters E_{htc}, R, and T_{Ar} are obtained. It can be seen that the model is quite robust and the following discussions should not be much influenced by the uncertainty of the assumed parameters.

IV. RESULTS

A. Modeling results

Taking the corresponding experimental discharge voltages and currents as the input parameters of the model, the MPPMS discharge processes in the pressure range of 0.1–0.7 Pa are modeled by fitting the calculated discharge currents to reproduce the experimental discharge currents. At all pressures from 0.1 to 0.7 Pa, the best fit of $\omega_{ge}\tau_c$ is around 16, in the range of "Bohm-like" diffusion of $8 < \omega_{ge}\tau_c < 30$ in the confined plasma.[44,48] Fig. 8 illustrates the modeled electron densities and temperatures of Ar/Cu MPPMS discharges during the modulated macropulses of 700 μs at different pressures of 0.1–0.7 Pa. The electron densities n_e at all pressures increase, and the electron temperature T_e at 0.1 Pa decreases from the weakly to the strongly ionized period, as
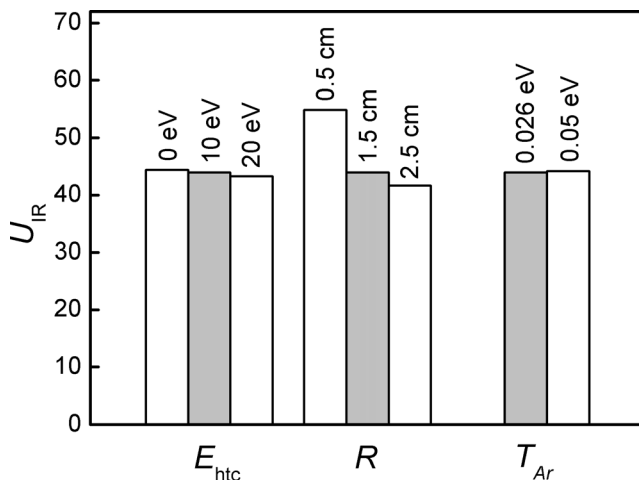

FIG. 7. Sensitivity analysis of the modeling at 0.3 Pa by varying the assumed parameters in the ranges of $0 \, eV < E_{htc} < 20 \, eV$, $0.5 \, cm < R < 2.5 \, cm$, and $0.026 \, eV < T_{Ar} < 0.05 \, eV$. Each time there is one parameter varied while the others kept at their nominal values, which are represented by the shaded columns.
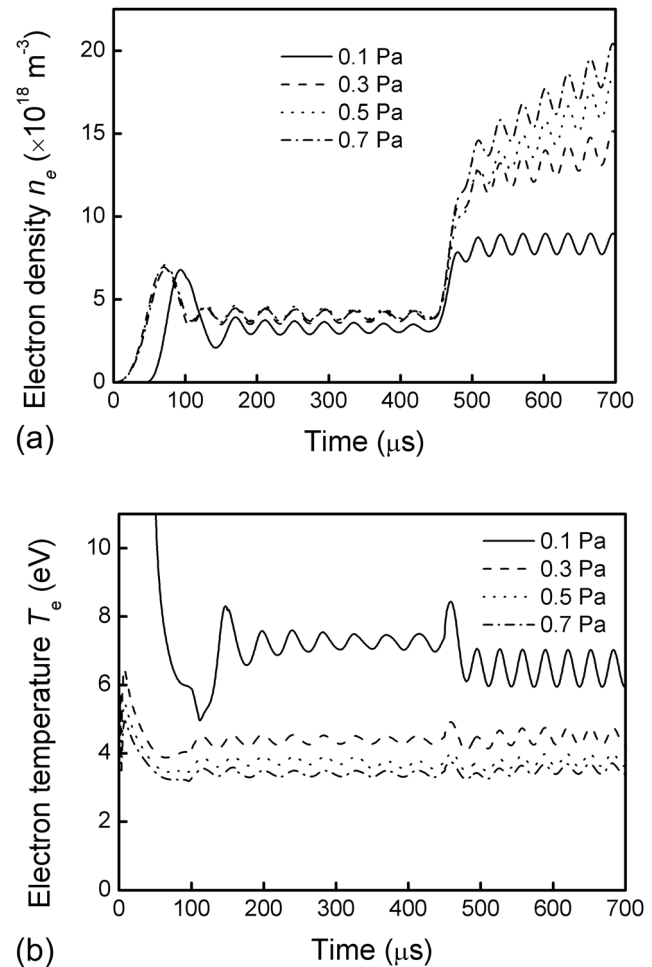

FIG. 8. Modeled electron densities and temperatures of Ar/Cu MPPMS discharges during the modulated macropulses of 700 μs at different pressures of 0.1–0.7 Pa.

well as from the low pressure of 0.1 Pa to the high pressure of 0.7 Pa. Similar features have been observed by plasma diagnostics in MPPMS discharges.[49,50] The behavior of n_e is similar to the discharge current, due to the variation of n_e influences the ion generation and thus the current on the target is changed proportionally. With increasing the pressure from 0.1 to 0.7 Pa, n_e during the strongly ionization period goes up from $8 \times 10^{18} \, m^{-3}$ to near $2 \times 10^{19} \, m^{-3}$ since there is more gas can be ionized. A jump appears between 0.1 and 0.3 Pa, owing to the number density of Ar is three times higher and much more electron-atom impact ionizations at 0.3 Pa. However, T_e has an opposite trend as n_e, due to the increase of n_e enhances the sputtering process and the resulting increased species cool the electrons through collisions. Similarly, a significant drop of T_e appears between 0.1 and 0.3 Pa, which decreases from 6–8 eV to around 4 eV due to the electrons undergo more collisions and drop more energy at higher pressures.

Fig. 9 shows the modeled potential drops across the ionization region U_{IR} of Ar/Cu MPPMS discharges during the modulated macropulses of 700 μs at different pressures of 0.1–0.7 Pa. The modeled potential drops U_{IR} of about 35–60 V correspond to the 10%–15% of the applied discharge voltage U_D of about 400 V. The value of U_{IR} during
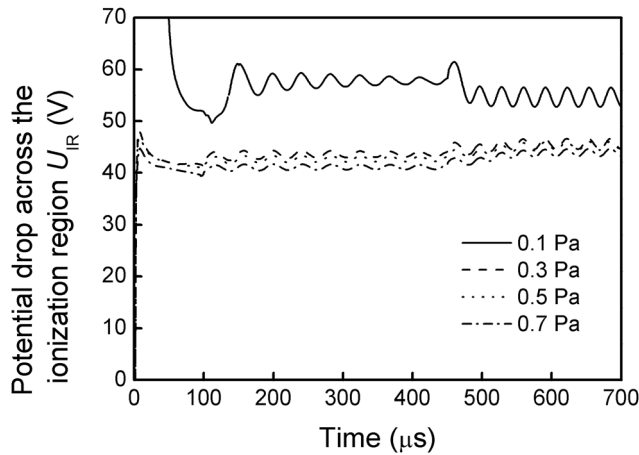
FIG. 9. Modeled potential drops across the ionization region U_{IR} of Ar/Cu MPPMS discharges during the modulated macropulses of 700 μs at different pressures of 0.1–0.7 Pa.

the overall macropulse at each pressure is relatively stable and drops at higher pressures, especially between 0.1 and 0.3 Pa, which is consistent with the observation of n_e and T_e. The decrease of U_{IR} with increasing the pressure has been observed in conventional dcMS[51] and in HiPIMS discharges,[44] since a negative space charge is established in the ionization region and increases with decreasing the pressure.

Once the potential drop U_{IR} is obtained, F_{PWR} and β_{Cu}^+ can be calculated based on the Eqs. (2) and (4). Fig. 10 shows the modeled effective power transfer coefficients F_{PWR} and Cu ion return fractions β_{Cu}^+ of Ar/Cu MPPMS discharges during the modulated macropulses of 700 μs at different pressures of 0.1–0.7 Pa. It can be observed that the oscillations of F_{PWR} match well with U_{IR}, and the values decrease during strongly ionized periods and at higher pressures. These decreases should be due to the increase of U_D over the strongly ionized periods with nearly constant U_{IR} and the decrease of U_{IR} at higher pressures, both result in the reduction of Ohm heating in the ionization region, which is the predominant heating mechanism in HiPIMS discharges.[36] The Cu ion return fraction β_{Cu}^+, as shown in Fig. 10, has a same trend as U_{IR} since more ions are attracted back at higher U_{IR}.

Fig. 11 shows the modeled Cu ionization fractions of Ar/Cu MPPMS discharges during the modulated macropulses of 700 μs at different pressures of 0.1–0.7 Pa. The ionization fraction of Cu is assumed as $n_{Cu}^+/(n_{Cu}^+ + n_{Cu})$, which goes up from 20%–45% during the weakly ionized period to 50%–60% during the strongly ionized period, due to the increased input power enhancing the ionization process. The ionization fraction decreases with increasing the pressure since the ion return fraction is decreased as shown in Fig. 10, and the ionized species are diluted by the increased sputtered species. The significant change of internal plasma parameters between 0.1 and 0.3 Pa shown above is believed to be the main reason of the observed structure zone transition of the deposited thin films as will be shown in Sec. IV B.

B. Experimental results

Fig. 12 shows the outer surface and cross-section of SEM images of Cu thin films deposited at different pressures

(a)

(b)
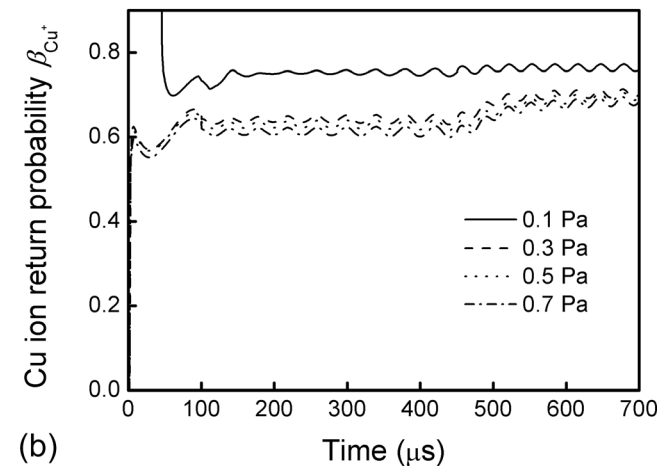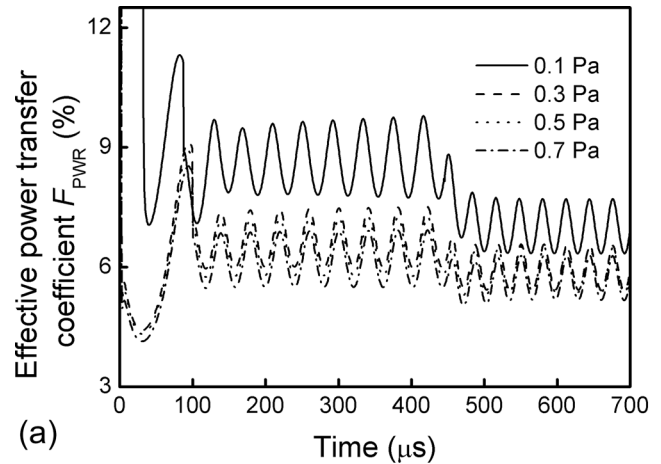
FIG. 10. Modeled effective power transfer coefficients F_{PWR} and Cu ion return fractions β_{Cu}^+ of Ar/Cu MPPMS discharges during the modulated macropulses of 700 μs at different pressures of 0.1–0.7 Pa.

from 0.1 to 0.7 Pa. The surface morphology becomes rougher and the pattern transforms from fine granular structure to coarse and crack visible structure with increasing the pressure. At relatively low pressure of 0.1 Pa, the cross-section of SEM shows a dense thin film with equiaxed grains and
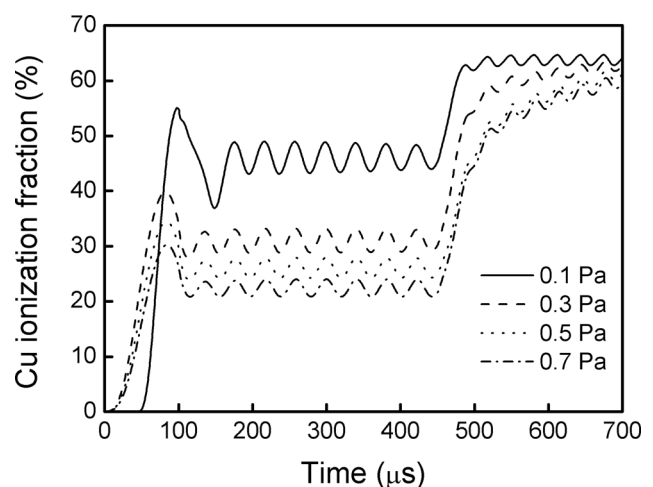
FIG. 11. Modeled Cu ionization fractions of Ar/Cu MPPMS discharges during the modulated macropulses of 700 μs at different pressures of 0.1–0.7 Pa.

Outer surface   **Cross-section**
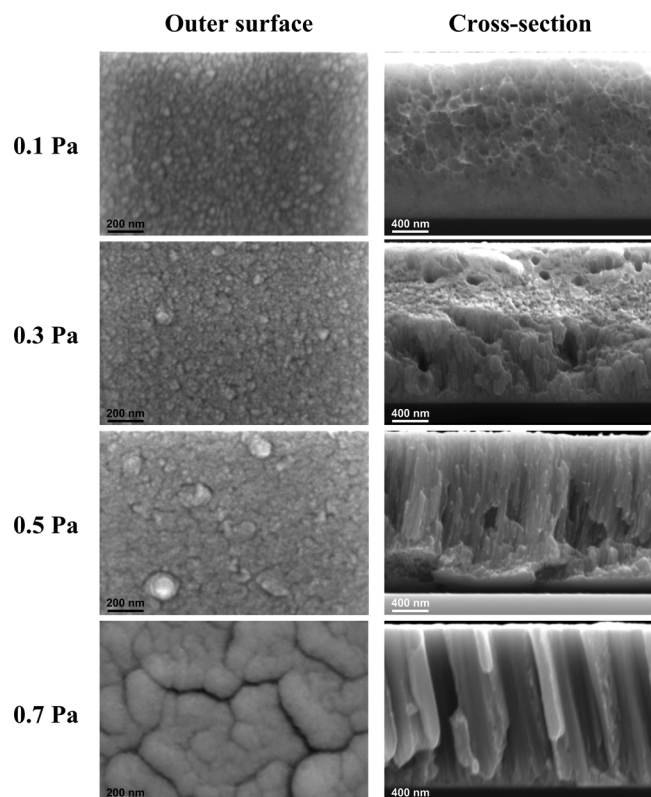
FIG. 12. Outer surface and cross-section of SEM images of Cu thin films deposited at different pressures of 0.1–0.7 Pa.

unclear grain boundaries. At 0.3 Pa, the short columnar grains appear near the bottom of the thin film with voids in different size. The columnar grains are much longer at 0.5 Pa and even penetrate through the thin film at 0.7 Pa, and voids appear at both pressures as well. The seemingly increased columnar width at 0.7 Pa, however, cannot be identified as the actual grain size due to the resolution limitation of the SEM images, and a more detailed structure should be analyzed by TEM.

Fig. 13 shows the cross-section of TEM images of Cu thin films deposited at different pressures from 0.1 to 0.7 Pa. A void free structure is shown at 0.1 Pa, with a wide distribution of grain size varying from tens to hundreds of nanometers, and some parts of the image show equiaxed grains. At 0.3 Pa, a relatively dense columnar grain structure with voids of nanoscale formed in the grain boundaries, the average columnar width is about 25 nm. The voids in the grain boundaries increase significantly at 0.5 Pa, albeit with little change in the grain size. Comparing with Fig. 12, it can be seen that the columnar grains at 0.7 Pa are not single grains but composed of finer columnar grains with unclear boundaries. Following the structure zone diagram (SZD),[11,52] with increasing the pressure, a transition from a void free structure with a wide distribution of grain size (zone T) at 0.1 Pa into an underdense structure with a fine fiber texture (zone 1) at 0.3–0.7 Pa is observed.

Typical x-ray diffraction patterns of Cu thin films deposited at different pressures from 0.1 to 0.7 Pa are shown in Fig. 14. Strong (111) preferred orientations are observed at all pressures, due to the (111) plane is the densest plane with
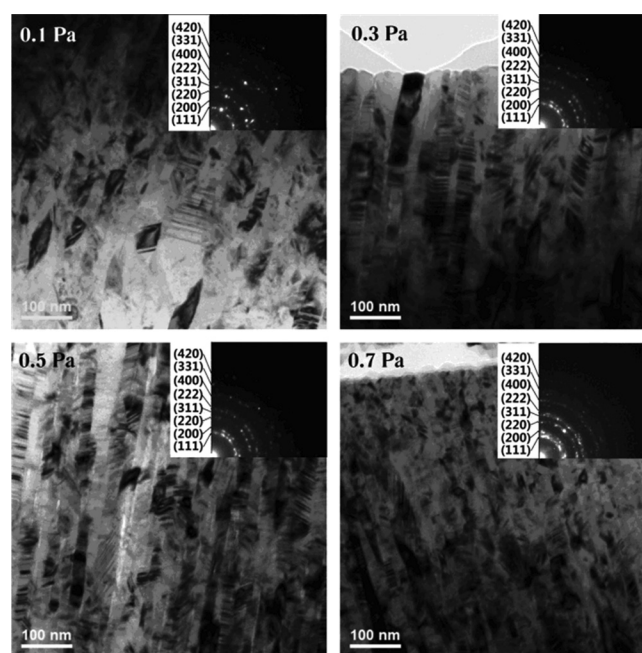

FIG. 13. Cross–section of TEM images of Cu thin films deposited at different pressures of 0.1–0.7 Pa.

the lowest surface energy in the fcc metal thin films.[53] The peak intensity ratios of I(111)/I(200) at different pressures are shown in Fig. 14, which increases in the pressure range from 0.1 to 0.5 Pa, then decreases at 0.7 Pa. Fig. 14 also shows that with increasing the pressure from 0.1 to 0.7 Pa, the calculated grain size of the deposited Cu thin films using the Scherrer formula is decreased, which is consistent with the TEM observation.

V. DISCUSSION

In the MPPMS process, the ionized species generated in the ionization region transport to the surrounding bulk plasma, travel through the sheath, and deposit on the substrate. The kinetic and potential energies of arriving ions are of great importance for the thin film growth. However, due to the many controllable process parameters and the highly ionized deposition flux, the SZD proposed by Thornton[30] is not appropriate to describe the microstructure evolution in MPPMS. In this work, following the extended SZD by Anders,[52] the plasma-dependent deposition parameters directly related to the thin film growth processes, i.e., the kinetic energy of arriving ions and the substrate temperature, which will be estimated by the internal plasma parameters, are adopted to describe their influence on the microstructure of deposited thin films rather than the primary process parameters. Due to the necessary simplifications made for the actual processes, the microstructure evolution of the thin film presented by an SZD must be qualitative. Moreover, the modeling results obtained from the global model is limited quantitative. The transport process of ionized species towards the substrate through the bulk plasma is thereby not considered, only a quantitative estimation of the energy of arriving ions and the substrate temperature is given by varying the internal plasma parameters with the pressure.
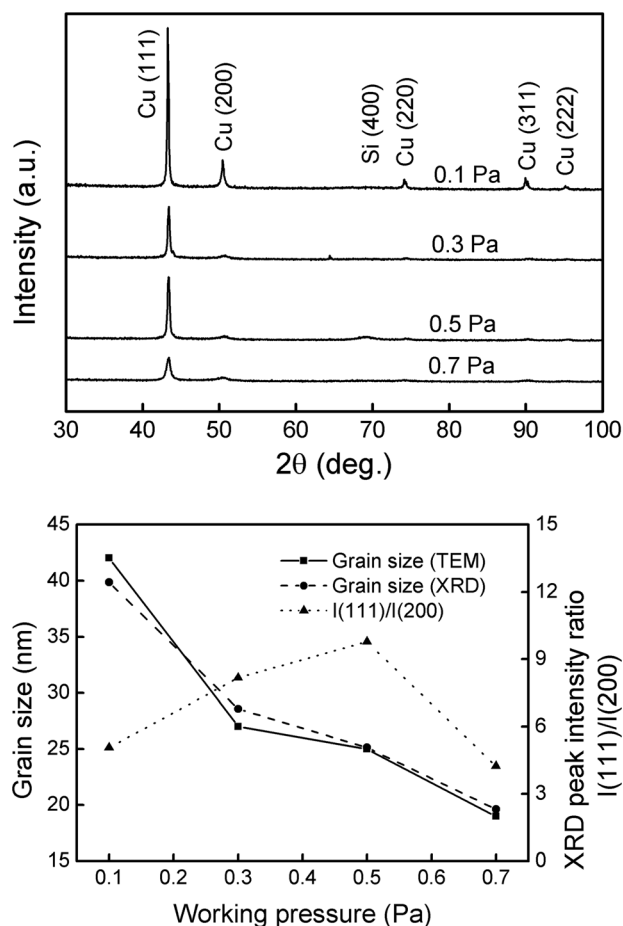
FIG. 14. XRD patterns, grain sizes, and XRD peak intensity ratios I(111)/I(200) of Cu thin films deposited at different pressures of 0.1–0.7 Pa.

Together with the extended SZD, the microstructure transition of the deposited Cu thin films with the pressure is explained.

The influence of the internal plasma parameters during discharges on the energy of arriving ions and the substrate temperature is estimated through the following two approaches: (i) the ionized species in the bulk plasma deposit on the substrate with the kinetic energy mainly obtained from the sheath region, which is estimated by the floating potential U_f; and (ii) due to the substrate is not heated by an external source, the necessary energy for the substrate temperature increase comes entirely from the input power of MPP power supply, and F_{PWR}, which represents the power fraction that effectively heats the electrons and maintains the discharge, is adopted to estimate the substrate heating at different pressures. The details of the estimation are as follows.

The kinetic energy of arriving ions includes an initial energy from the plasma and the energy obtained from the potential drop of the sheath. Without applying negative bias, a floating potential is established on the substrate and accelerates the arriving ions, which can be derived as $U_f = -T_e \ln(M/2\pi m)^{1/2}$. M and m are the mass of the ion and the electron, respectively. The electron temperature T_e in Fig. 8 is averaged over the on-time of the macropulse and weighted by n_e, to estimate the average floating potential. Due to the strong magnetic confinement of electrons near the

target allowing only the higher energy electrons to escape, the average T_e might be even higher further from the target.[49] However, the same trend of T_e as changing the pressure could be expected both near the substrate and in the ionization region, and the latter is thereby adopted as an approximate estimate. Ignoring the initial energy before entering the substrate sheath, e.g., gained from the potential double layer caused by spokes,[54] the kinetic energy of arriving ions can be estimated by the floating potential U_f. Fig. 15 illustrates the calculated floating potential U_f averaged over the modulated macropulses of 700 μs at different pressures of 0.1–0.7 Pa. Apparently, U_f has the same tendency as T_e, which decreases at higher pressures, implies that the kinetic energy of arriving ions decreases with increasing the pressure. Similar floating potentials on the substrate have been observed in MPPMS discharges, e.g., $T_e = 6$–11 eV at 0.13 Pa,[49] $U_f = 10$–15 V at 0.53 Pa,[50] and 15–20 V at 0.67 Pa.[55] Correspondingly, the floating potential in Fig. 15 is about 33 V derived from T_e of 6–8 eV at 0.1 Pa, 18 V at 0.5 Pa, and 17 V at 0.7 Pa.

The substrate temperature includes the growth temperature of deposited thin films and the temperature variation resulted from the potential energy of the arriving species. For neutrals, the potential energy is the cohesive energy, and for ions the ionization energy reduced by the work function of the electron is included as well. HiPIMS has been observed to deliver a relatively low thermal flux to the substrate, which is beneficial to the deposition on thermally sensitive substrates.[56] The thermal flux to the substrate includes sputtered atoms, electrons at the substrate, plasma irradiation, and thermal irradiation.[57] All these energies are provided by the MPPMS power supply, which remains constant at an average power of 2 kW in this work. However, a large portion of the energy are returned to the target by the ion current and removed by the cooling system. Therefore, the thermal flux to the substrate, which influences the substrate temperature, is expected to be dependent on the effective input power. The variation of the substrate temperature is supposed to have the same trend as the effective power transfer coefficient F_{PWR}, which represents the power fraction that effectively heats the electrons and maintains the discharge. Fig. 16 illustrates the calculated effective power
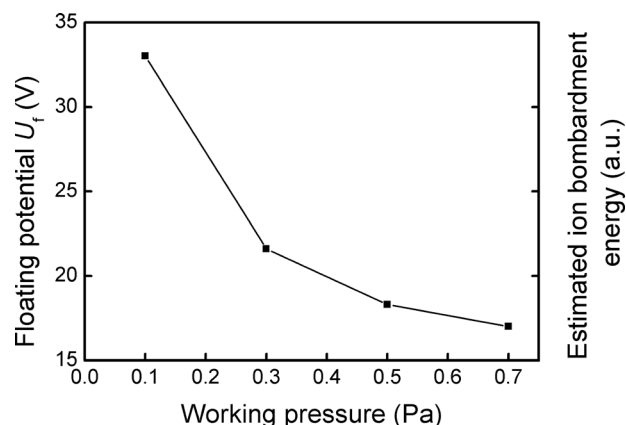

FIG. 15. Calculated floating potential U_f averaged over the modulated macropulses of 700 μs at different pressures of 0.1–0.7 Pa.
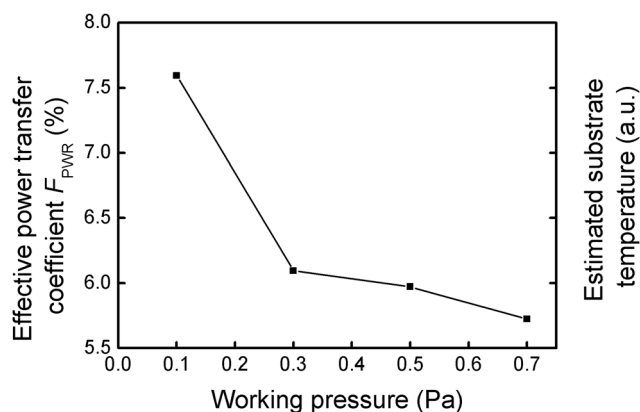
FIG. 16. Calculated effective power transfer coefficient F_{PWR} averaged over the modulated macropulses of 700 μs at different pressures of 0.1–0.7 Pa.

transfer coefficient F_{PWR} averaged over the modulated macropulses of 700 μs at different pressures of 0.1–0.7 Pa. It can be seen that with the increase of the pressure, F_{PWR} decreases owing to the reduced U_{IR}, implies that the substrate temperature decreases with increasing the pressure.

As shown in Figs. 15 and 16, with increasing the pressure from 0.1 to 0.7 Pa, both the kinetic energy of arriving ions estimated by U_f and the substrate temperature estimated by F_{PWR} decrease, which is consistent with the structure zone transition of deposited Cu thin films from zone T into zone 1 observed in Figs. 12 and 13, owing to the decreased surface diffusion. Particularly, with increasing the pressure from 0.1 to 0.3 Pa, the jump of internal plasma parameters results in a drop in the energy of arriving ions and the substrate temperature, corresponding to the significant microstructure evolution of deposited Cu thin films from a dense and void free structure (zone T) at 0.1 Pa into a columnar grain structure with voids of nanoscale formed in the grain boundaries (zone 1) at 0.3 Pa. At 0.1 Pa, the kinetic energy of arriving ions and the substrate temperature are relatively high, the bulk diffusion is negligible but the adatom mobility on the surface is significant. With increasing the pressure from 0.1 to 0.7 Pa, the ion-to-metal flux ratio J_i/J_M incident at the growing thin film surface decreases from 3.71 to 2.45, which can be estimated since the ion flux out of the ionization region is governed by Bohm velocity, $J_i = (1 - \beta_{Cu}^+)u_B n_{Cu}^+/2$, and the neutral flux by the mean thermal velocity of the gas, $J_M = 0.25(8kT_{Ar}/m_{Cu})^{1/2}n_{Cu}$.[12] The increased fraction of neutral flux in the deposition flux with a wider angular distribution due to more collisions at higher pressures results in an increased atomic shadowing. In addition, the surface diffusion is limited since both the kinetic energy of arriving ions and the substrate temperature are reduced at higher pressures. Therefore, there are more intercolumnar voids appearing and the surface is rougher with increasing the pressure. At higher film growth temperatures, the grains are enlarged due to the grain coarsening during the coalescence of small islands,[11] and the increase of adatom mobility dominates the increase of defects and renucleation rates induced by ion bombardment.[52] Recalling that the film growth temperature decreases with increasing the pressure, meaning the grain size should be decreased at higher pressures, which is consistent with the experimental results as shown in Fig. 14.

Fig. 14 also shows the increased peak intensity ratios of I(111)/I(200) with increasing the pressure from 0.1 to 0.5 Pa. Huang *et al.*[58] have found that during the sputtering process of depositing fcc Ag thin films, the auxiliary bombardment of Ar^+ ions reduce the preferred orientation, which was even less with increasing the energy of Ar^+ ions. Bradley *et al.*[59] argued that with the ion auxiliary bombardment, the development of preferred orientation during thin film growth is related to the different sputtering yields for different orientations. For fcc metals, the sputtering yield is (110) < (100) < (111), therefore the ratio of I(111)/I(200) increases with increasing the ion energy and the ion-to-neural ratio of deposition flux, which has been observed in fcc metals such as Pt[60] and Ag.[61] Simulation of the texture development by ion beam assisted deposition of fcc Al was performed as well,[62] and a reduction of (111) orientation was observed. However, as shown in Fig. 14, at higher pressure of 0.7 Pa, the ratio of I(111)/I(200) is decreased, may be due to the thin film growth in zone 1 with a negligible adatom diffusion develops an underdense structure with voids and cracks and results in a low crystallinity.

Though the various modeling approaches have been used to describe the magnetron discharges, several challenges remain for the simulation of high density magnetized plasmas.[63] In order to understand the variation of the internal plasma parameters with the pressure, a volume-averaged global model is adopted in this work, with considering the kinetic effects of energetic electrons both in the power coupling to the discharge and in the ionization processes. The pressure range of 0.1–0.7 Pa is a relatively small interval with respect to the level of accuracy of a global model, particularly of a fitted parameter model. However, the variation of modeled internal plasma parameters with the pressure is well correlated with the experimentally observed microstructure evolution of deposited Cu thin films by the extended SZD, especially in the pressure range of 0.1–0.3 Pa, where both the modeling and the experimental results present a significant change. The variation of grain size and peak intensity ratio with the pressure is well understood as well, suggesting that this approach is acceptable for the understanding of the characteristics of MPPMS discharges, as well as its correlation with the microstructure and texture of deposited Cu thin films.

VI. CONCLUSIONS

(i)   A time-dependent global plasma model is developed for MPPMS discharges based on a volume-averaged global description of the ionization region, considering the loss of electrons by cross-B diffusion. The temporal variations of internal plasma parameters, such as number densities of each species, electron temperature, ionization fraction, and potential drop across the ionization region, are obtained by fitting the model to duplicate the experimental discharge data at different pressures from 0.1 to 0.7 Pa.

(ii)   Cu thin films are deposited by MPPMS at the corresponding pressures. The surface morphology, grain size and orientation, and microstructure of the deposited thin films are investigated by SEM, TEM, and XRD. A transition from a void free structure with a

wide distribution of grain size (zone T) into an under-dense structure with a fine fiber texture (zone 1) of the deposited thin films is identified with increasing the pressure from 0.1 to 0.7 Pa. The intercolumnar voids increase, the surface morphology becomes rougher, and the pattern transforms from fine granular structure to coarse and crack visible structure with increasing the pressure. The calculated grain size of the deposited Cu thin films using the Scherrer formula decreases at higher pressures, which is consistent with the TEM observation.

(iii) The internal plasma parameters are used to estimate the parameters directly related to the thin film growth processes, which are adopted in the extended SZD, i.e., the kinetic energy of arriving ions and the substrate temperature, to describe their influence on the microstructure of deposited thin films. As increasing the pressure from 0.1 to 0.7 Pa, both the kinetic energy of arriving ions and the substrate temperature decrease, corresponding to the observed transition from zone T into zone 1, as well as the increase of intercolumnar voids and the surface roughness of the deposited thin films. The grain size increases at lower pressures due to the grain coarsening during the coalescence and the increased adatom mobility at higher film growth temperatures. The increase of preferred (111) orientation with increasing the pressure from 0.1 to 0.5 Pa may be owing to the relatively higher sputtering yield of (111) orientation.

(iv) The microstructure and texture transition of thin films are well-explained by the extended SZD, suggesting that the primary plasma processes are properly incorporated in the model. The results contribute to the understanding of the characteristics of MPPMS discharges, as well as its correlation with the microstructure and texture of deposited Cu thin films.

APPENDIX: RATE COEFFICIENTS AND FLUXES OF SPECIES

To establish the particle balance equations for each species and the energy balance equation for the system, it is necessary to know the selected reactions and the corresponding rate coefficients, which are shown in Table I.

The diffusional flux of Ar from the surroundings is considered as the net flow across the ionization region boundary

$$\Gamma_{\text{Ar,diff}} = \frac{n_{\text{Ar0}} - n_{\text{Ar}}}{4} u_{T_{\text{Ar}}}, \tag{A1}$$

where n_{Ar0} and n_{Ar} are the number densities of Ar in the surroundings and in the ionization region, $u_{T\text{Ar}} = (8kT_{\text{Ar}}/\pi m_{\text{Ar}})^{1/2}$ is the average velocity of Ar at a temperature $T_{\text{Ar}} \approx 300\,\text{K}$, k is the Boltzmann constant, and m_{Ar} is the mass of Ar atom.

For metastable Ar^{m},

$$\Gamma_{\text{Ar}^{\text{m}},\text{diff}} = \frac{n_{\text{Ar}^{\text{m}}} u_{T_{\text{Ar}^{\text{m}}}}}{4}. \tag{A2}$$

The fluxes of sputtering wind composed of Cu and Cu^{+} are

$$\begin{aligned} \Gamma_{\text{Cu},0} &= \frac{u_{T_{\text{Cu}}} n_{\text{Cu}}}{4}, \\ \Gamma_{\text{Cu}^{+},0} &= \frac{u_{T_{\text{Cu}}} n_{\text{Cu}^{+}}}{4}, \end{aligned} \tag{A3}$$

where $u_{T\text{Cu}} = (3kT_{\text{Cu}}/m_{\text{Cu}})^{1/2}$ is the root mean square velocity of Cu. The collision probability with Ar in the ionization region is

$$F_{\text{coll}} = 1 - \exp\left(-\frac{R}{\lambda_{\text{coll}}}\right), \tag{A4}$$

where λ_{coll} is the mean free path for Cu-Ar momentum exchange collision

$$\lambda_{\text{coll}} = \frac{1}{\sigma_{\text{m}}(n_{\text{Ar}} + n_{\text{Ar}^{\text{m}}} + n_{\text{Ar}^{\text{H}}})}, \tag{A5}$$

TABLE I. Principal rate coefficients for Ar/Cu plasma.

Reaction	Rate coefficient (m^3 s^{-1})	Threshold (eV)	Reference
$e + Ar \rightarrow Ar^+ + 2e$	$k_{\text{iz}} = 2.3 \times 10^{-14} T_e^{0.59} \exp(-17.44/T_e)$	15.76	34
$e^H + Ar \rightarrow Ar^+ + 2e$	$k_{\text{iz}}^H = 8 \times 10^{-14} T_e^{0.16} \exp(-27.53/T_e)$	15.76	64 and 65
$e + Ar \rightarrow Ar^m + e$	$k_{\text{ex}} = k_{\text{ex}}^H = 2.5 \times 10^{-15} T_e^{0.74} \exp(-11.56/T_e)$	11.56	34
$e^H + Ar \rightarrow Ar^m + e$	$k_{\text{ex}}^H = 3.85 \times 10^{-14} T_e^{-0.68} \exp(-22.32/T_e)$	11.56	64 and 65
$e + Ar \rightarrow Ar + e$ (elastic)	$k_{\text{el}} = 2.336 \times 10^{-14} T_e^{1.609}$ $\times e^{0.0618(\ln T_e)^2 - 0.1171(\ln T_e)^3}$		47
$e + Ar^m \rightarrow Ar + e$	$k_{\text{dex}} = 4.3 \times 10^{-16} T_e^{0.74}$	−11.56	34
$e + Ar^m \rightarrow Ar^+ + 2e$	$k_{\text{miz}} = 6.8 \times 10^{-15} T_e^{0.67} \exp(-4.2/T_e)$	4.2	34
$e^H + Ar^m \rightarrow Ar^+ + 2e$	$k_{\text{miz}}^H = 5.7 \times 10^{-13} T_e^{-0.33} \exp(-6.82/T_e)$	4.2	66
$e + Cu \rightarrow Cu^+ + 2e$	$k_{\text{Miz}} = k_{\text{Miz}}^H = 3.898 \times 10^{-14}$ $\times T_e^{0.484} \exp(-7.1344/T_e)$	7.68	12
$e + Cu \rightarrow Cu + e$ (elastic)	$k_{\text{el}} = 2.336 \times 10^{-14} T_e^{1.609}$ $\times e^{0.0618(\ln T_e)^2 - 0.1171(\ln T_e)^3}$		67
$Ar^m + Cu \rightarrow Ar + Cu^+ + e$	$k_{\text{P}} = 2.36 \times 10^{-16}$	−4.46	68
$Ar^+ + Cu \rightarrow Ar + Cu^+$	$k_{\text{chexc}} = 2 \times 10^{-16}$		69

where $\sigma_{\mathrm{m}} = \pi(a_1 + a_2)^2$ is the cross-section of Cu-Ar collision estimated by the hard sphere model, $a_1 = 1.88\,\text{Å}$ and $a_2 = 1.4\,\text{Å}$ are the atomic radii of Ar and Cu, respectively. For simplicity, the λ_{coll} between Cu^+ and Ar is assumed to be the same as Cu-Ar collision. The minimum of λ_{coll} is, at the maximal pressure of 0.7 Pa without considering the rarefaction, about 1.7 cm, which is larger than the scale of the ionization region R. The collision fraction of the sputtering wind of Cu and Cu^+ in the ionization region is

$$\Gamma_{\mathrm{Cu,coll}} = \left(\Gamma_{Cu^+,0} + \Gamma_{\mathrm{Cu},0}\right)F_{\mathrm{coll}}$$
$$= \frac{n_{\mathrm{Cu}} + n_{Cu^+}}{4} u_{T_{\mathrm{Cu}}}\left(1 - \exp\left(-\frac{R}{\lambda_{\mathrm{coll}}}\right)\right), \quad (A6)$$

and the diffusion flux of Cu out of the ionization region without collision is

$$\Gamma_{\mathrm{Cu,diff}} = \Gamma_{\mathrm{Cu},0}(1 - F_{\mathrm{coll}}) = \frac{n_{\mathrm{Cu}} u_{T_{\mathrm{Cu}}}}{4} e^{-R/\lambda_{\mathrm{coll}}}. \quad (A7)$$

Assuming the ion fluxes across the IR surface with a Bohm velocity, the fluxes of Ar^+ and Cu^+ leaving the IR can be expressed as

$$\Gamma_{Ar^+} = 0.4 n_{Ar^+} u_{B,Ar},$$
$$\Gamma_{Cu^+} = 0.4 n_{Cu^+} u_{B,Cu}. \quad (A8)$$

[1]V. Kouznetsov, K. Macak, J. M. Schneider, U. Helmersson, and I. Petrov, Surf. Coat. Technol. **122**, 290 (1999).
[2]J. T. Gudmundsson, N. Brenning, D. Lundin, and U. Helmersson, J. Vac. Sci. Technol. A **30**, 030801 (2012).
[3]J. Alami, J. T. Gudmundsson, J. Bohlmark, J. Birch, and U. Helmersson, Plasma Sources Sci. Technol. **14**, 525 (2005).
[4]J. Gudmundsson, P. Sigurjonsson, P. Larsson, D. Lundin, and U. Helmersson, J. Appl. Phys. **105**, 123302 (2009).
[5]A. Anders, Surf. Coat. Technol. **205**, S1 (2011).
[6]J. Bohlmark, J. Alami, C. Christou, A. P. Ehiasarian, and U. Helmersson, J. Vac. Sci. Technol. A **23**, 18 (2005).
[7]E. Oks and A. Anders, J. Appl. Phys. **105**, 093304 (2009).
[8]J. Alami, P. Persson, D. Music, J. Gudmundsson, J. Bohmark, and U. Helmersson, J. Vac. Sci. Technol. A **23**, 278 (2005).
[9]K. Bobzin, N. Bagcivan, P. Immich, S. Bolz, R. Cremer, and T. Leyendecker, Thin Solid Films **517**, 1251 (2008).
[10]M. Balzer and M. Fenker, Surf. Coat. Technol. **250**, 37 (2014).
[11]I. Petrov, P. B. Barna, L. Hultman, and J. E. Greene, J. Vac. Sci. Technol. A **21**, S117 (2003).
[12]M. Samuelsson, D. Lundin, J. Jensen, M. Raadu, J. Gudmundsson, and U. Helmersson, Surf. Coat. Technol. **205**, 591 (2010).
[13]A. Ehiasarian, J. Wen, and I. Petrov, J. Appl. Phys. **101**, 054301 (2007).
[14]N. Brenning, C. Huo, D. Lundin, M. A. Raadu, C. Vitelaru, G. D. Stancu, T. Minea, and U. Helmersson, Plasma Sources Sci. Technol. **21**, 025005 (2012).
[15]A. Anders, J. Vac. Sci. Technol. A **28**, 783 (2010).
[16]J. Alami, K. Sarakinos, G. Mark, and M. Wuttig, Appl. Phys. Lett. **89**, 154104 (2006).
[17]R. Chistyakov, B. Abraham, and W. D. Sproul, in *49th Annual Technical Conference Proceedings* (Society of Vacuum Coaters, Washington, D. C., 2006), p. 88.
[18]J. Lin, W. Sproul, J. Moore, S. Lee, and S. Myers, Surf. Coat. Technol. **205**, 3226 (2011).
[19]F. Papa, H. Gerdes, R. Bandorf, A. Ehiasarian, I. Kolev, G. Braeuer, R. Tietema, and T. Krug, Thin Solid Films **520**, 1559 (2011).
[20]J. Lin, J. Moore, W. Sproul, B. Mishra, J. Rees, Z. Wu, R. Chistyakov, and B. Abraham, Surf. Coat. Technol. **203**, 3676 (2009).
[21]S. Myers, J. L. Lin, R. M. Souza, W. D. Sproul, and J. J. Moore, Surf. Coat. Technol. **214**, 38 (2013).
[22]J. L. Lin, N. Y. Zhang, Z. L. Wu, W. D. Sproul, M. Kaufman, M. K. Lei, and J. J. Moore, Surf. Coat. Technol. **228**, S601 (2013).
[23]J. Paulitsch, C. Maringer, and P. H. Mayrhofer, Tribol. Lett. **46**, 87 (2012).
[24]J. L. Lin, B. Wang, Y. X. Ou, W. D. Sproul, I. Dahan, and J. J. Moore, Surf. Coat. Technol. **216**, 251 (2013).
[25]M. Hala, J. Capek, O. Zabeida, J. E. Klemberg-Sapieha, and L. Martinu, Surf. Coat. Technol. **206**, 4186 (2012).
[26]D. Depla and W. P. Leroy, Thin Solid Films **520**, 6337 (2012).
[27]K. A. Aissa, A. Achour, J. Camus, L. Le Brizoual, P. Y. Jouan, and M. A. Djouadi, Thin Solid Films **550**, 264 (2014).
[28]S. Nakao, K. Yukimura, H. Ogiso, S. Nakano, and T. Sonoda, Vacuum **89**, 261 (2013).
[29]A. N. Reed, M. A. Lange, C. Muratore, J. E. Bultman, J. G. Jones, and A. A. Voevodin, Surf. Coat. Technol. **206**, 3795 (2012).
[30]J. A. Thornton, J. Vac. Sci. Technol. **11**, 666 (1974).
[31]A. Rauch, R. J. Mendelsberg, J. M. Sanders, and A. Anders, J. Appl. Phys. **111**, 083302 (2012).
[32]D. Christie, J. Vac. Sci. Technol. A **23**, 330 (2005).
[33]J. Vlcek and K. Burcalova, Plasma Sources Sci. Technol. **19**, 065010 (2010).
[34]M. Raadu, I. Axnas, J. Gudmundsson, C. Huo, and N. Brenning, Plasma Sources Sci. Technol. **20**, 065007 (2011).
[35]C. Q. Huo, M. A. Raadu, D. Lundin, J. T. Gudmundsson, A. Anders, and N. Brenning, Plasma Sources Sci. Technol. **21**, 045004 (2012).
[36]C. Q. Huo, D. Lundin, M. A. Raadu, A. Anders, J. T. Gudmundsson, and N. Brenning, Plasma Sources Sci. Technol. **22**, 045005 (2013).
[37]C. Q. Huo, D. Lundin, M. A. Raadu, A. Anders, J. T. Gudmundsson, and N. Brenning, Plasma Sources Sci. Technol. **23**, 025017 (2014).
[38]A. J. Lichtenberg and M. A. Lieberman, J. Appl. Phys. **87**, 7191 (2000).
[39]K. Tao, D. Mao, and J. Hopwood, J. Appl. Phys. **91**, 4040 (2002).
[40]S. Ashida, C. Lee, and M. A. Lieberman, J. Vac. Sci. Technol. A **13**, 2498 (1995).
[41]J. A. Hopwood, *Ionized Physical Vapor Deposition* (Academic Press, San Diego, 2000).
[42]J. Gudmundsson, J. Phys. Conf. Ser. **100**, 082013 (2008).
[43]J. W. Bradley, S. Thompson, and Y. A. Gonzalvo, Plasma Sources Sci. Technol. **10**, 490 (2001).
[44]A. Mishra, P. Kelly, and J. Bradley, Plasma Sources Sci. Technol. **19**, 045014 (2010).
[45]L. Meng, "Comparison of high power impulse magnetron sputtering and modulated pulsed power sputtering for interconnect metallization," Ph.D. thesis, University of Illinois at Urbana-Champaign, Urbana, USA, 2013.
[46]J. F. Ziegler, M. D. Ziegler, and J. P. Biersack, Nucl. Instrum. Methods B **268**, 1818 (2010).
[47]M. A. Lieberman and A. J. Lichtenberg, *Principles of Plasma Discharges and Materials Processing* (John Wiley & Sons Inc., New Jersey, 2005).
[48]B. Liebig and J. W. Bradley, Plasma Sources Sci. Technol. **22**, 045020 (2013).
[49]L. Meng, A. Cloud, S. Jung, and D. Ruzic, J. Vac. Sci. Technol. A **29**, 011024 (2011).
[50]B. Liebig, N. Braithwaite, P. Kelly, R. Chistyakov, B. Abraham, and J. Bradley, Surf. Coat. Technol. **205**, S312 (2011).
[51]T. A. van der Straaten, N. F. Cramer, I. S. Falconer, and B. W. James, J. Phys. D **31**, 177 (1998).
[52]A. Anders, Thin Solid Films **518**, 4087 (2010).
[53]H. Lee, S. S. Wong, and S. D. Lopatin, J. Appl. Phys. **93**, 3796 (2003).
[54]C. Maszl, W. Breilmann, J. Benedikt, and A. von Keudell, J. Phys. D **47**, 224002 (2014).
[55]J. Lin, J. Moore, W. Sproul, S. Lee, and J. Wang, IEEE Trans. Plasma Sci. **38**, 3071 (2010).
[56]G. West, P. Kelly, P. Barker, A. Mishra, and J. Bradley, Plasma Process. Polym. **6**, S543 (2009).
[57]S. D. Ekpe and S. K. Dew, J. Vac. Sci. Technol. A **20**, 1877 (2002).
[58]T. C. Huang, G. Lim, F. Parmigiani, and E. Kay, J. Vac. Sci. Technol. A **3**, 2161 (1985).
[59]R. M. Bradley, J. M. E. Harper, and D. A. Smith, J. Appl. Phys. **60**, 4160 (1986).
[60]B. J. Jiang, J. Jiang, C. X. Ren, X. H. Liu, X. Wang, T. Feng, Z. X. Zhang, Z. T. Song, and L. P. Zheng, Thin Solid Films **483**, 411 (2005).
[61]T. Feng, B. Y. Jiang, S. Zhuo, X. Wang, and X. H. Liu, Appl. Surf. Sci. **254**, 1565 (2008).

[62]L. Dong and D. J. Srolovitz, J. Appl. Phys. **84**, 5261 (1998).

[63]A. Bogaerts, E. Bultinck, I. Kolev, L. Schwaederle, K. Van Aeken, G. Buyle, and D. Depla, J. Phys. D **42**, 194018 (2009).

[64]N. J. Mason and W. R. Newell, J. Phys. B **20**, 1357 (1987).

[65]V. Puech and L. Torchin, J. Phys. D **19**, 2309 (1986).

[66]H. A. Hyman, Phys. Rev. A **20**, 855 (1979).

[67]S. Trajmar, W. Williams, and S. K. Srivastava, J. Phys. B **10**, 3323 (1977).

[68]A. Bogaerts, R. Gijbels, and R. J. Carman, Spectrochim. Acta B **53**, 1679 (1998).

[69]S. C. Rae and R. C. Tobin, J. Appl. Phys. **64**, 1418 (1988).